Nucleon direct-semidirect radiative capture with Skyrme-Hartree-Fock-BCS bound states

L. Bonneau,[1,*] T. Kawano,[1] T. Watanabe,[1,2] and S. Chiba[3]
[1]*Theoretical Division, Los Alamos National Laboratory, Los Alamos, New Mexico 87545, USA*
[2]*Department of Applied Quantum Physics and Nuclear Engineering, Kyushu University, 744 Motooka, Nishi-ku, Fukuoka 819-0395, Japan*
[3]*Advanced Science Research Center, Japan Atomic Energy Agency, Tokai, Ibaraki 319-1195, Japan*
(Received 6 February 2007; published 30 May 2007)

The nucleon direct-semidirect (DSD) capture cross sections are obtained by calculating a transition amplitude to the Hartree-Fock-BCS bound states. The radial matrix elements in the DSD amplitudes are calculated from the radial part of the single-particle wave functions. For deformed nuclei the single-particle states are expanded in the cylindrical harmonic-oscillator basis and then projected on the spherical harmonic-oscillator basis. The pairing correlations are treated in the BCS approach and the calculated spectroscopic factors are in fairly good agreement with experimental data in the even tin isotopes from ^{116}Sn to ^{124}Sn. The resulting DSD cross sections for the neutron capture by ^{208}Pb and ^{238}U are found to be in good agreement with the available experimental data. The calculations are also performed for the neutron capture on ^{122}Sn and ^{132}Sn isotopes that are important for the r-process in astrophysics.

DOI: 10.1103/PhysRevC.75.054618 PACS number(s): 24.10.Eq, 24.60.Dr, 21.60.Jz, 26.20.+f

I. INTRODUCTION

The nucleon radiative capture is one of the most important processes for nucleosynthesis calculations in astrophysics. The energy range of interest for the neutron capture process in astrophysical applications depends on the temperature of the Maxwell-Boltzmann velocity distribution [1]. Neutron capture cross sections of up to several MeV may meet astrophysical conditions in many cases. In this energy region, the statistical Hauser-Feshbach model with width fluctuation correction is known to be applicable [2] to calculate the astrophysical nuclear reaction rates, and extensive studies have been made (see Ref. [3], for example).

In compound nuclear reactions, the capture cross sections become very small when neutron inelastic channels open, because the neutron width Γ_n becomes much larger than the γ-ray width Γ_γ. For incident nucleon energies above 5 MeV or so, the capture process can be mainly described by the direct-semidirect (DSD) mechanism [4–7]. In this mechanism, the incident particle is captured directly in an unoccupied bound state (direct), or it excites a collective (giant dipole resonance) state and then is scattered into a bound state (semidirect). Within the perturbation theory, the transition probabilities of these processes involve radial wave functions and spectroscopic factors of the final states. The radial part of the wave function is often calculated with a single-particle model assuming that the potential has a spherical Woods-Saxon shape and the experimental spectroscopic factors S are used if available.

For astrophysical calculations, the experimental information on nuclear structure for unstable nuclei is often uncertain or unavailable. Therefore we have to estimate model parameters in a reasonable way to calculate the DSD cross section. For example, Goriely [8] estimated an energy-independent average value for C^2S (C being a coupling constant) from experimental spectroscopic factors for many nuclei.

In the present study, we apply the Hartree-Fock-BCS (HFBCS) model to determine the radial wave functions of the single-particle bound states and their associated occupation probabilities. We choose here the Skyrme interaction in the mean-field channel in two different parametrizations and the traditionally associated pairing interaction. Within the HFBCS approximation the spectroscopic factors are connected with the occupation probabilities for each single-particle orbit in a simple way [9,10]. The main interest of considering the HFBCS approach to nuclear structure here is that we can describe the ground-state properties of spherical as well as deformed nuclei (with axial symmetry assumed) in a predictive manner. Here we restrict ourselves to even-even targets. It is worth mentioning that one could also calculate the single-particle wave functions and occupancies within a microscopic-macroscopic approach where the single-particle potential is prescribed for a given nuclear shape [11].

The present article is organized as follows. After a brief description in Sec. II of the formalisms used to implement the DSD mechanism and to calculate the relevant nuclear structure properties in the HFBCS model, we present and discuss the results for the bound-state properties and the neutron capture cross sections for ^{208}Pb, ^{238}U, and ^{122,132}Sn in Sec. III. Finally we draw the main conclusions of this study in Sec. IV.

II. THEORETICAL FRAMEWORK

A. Direct-semidirect cross section

The DSD model for nucleon capture initially proposed by Brown [4] and Clement, Lane, and Rook [5] was later on extended to deformed nuclei by Boisson and Jang [12]. The procedure outlined by Boisson-Jang was then followed by several studies [13–15] to reproduce experimental capture cross sections for deformed nuclei. We recall it below to establish our notation.

*Electronic address: bonneau@lanl.gov

Let us consider an incident nucleon with wave number k_n and orbital and total angular momenta L and J, respectively. We denote by $R_{LJ}(r)$ the radial part of its distorted wave function calculated within the optical model. This nucleon is captured by an even-even target initially in its ground state (initial spin 0) and scattered into a bound state $|k\rangle$. With the assumption of axial symmetry for the deformed target, the single-particle $|k\rangle$ is an eigenstate of J_z, the projection on the symmetry axis of the angular momentum operator $\mathbf{J}^2$. The associated eigenvalue is denoted by K. The deformed single-particle state $|k\rangle$ is a superposition of eigenstates of the orbital and total angular momentum operators $\mathbf{L}^2$ and $\mathbf{J}^2$, respectively:

$$|k\rangle = \sum_{l,j} C_{lj}^{(k)} |ljK\rangle, \tag{1}$$

with

$$\mathbf{L}^2|ljK\rangle = l(l+1)\hbar^2|ljK\rangle, \tag{2}$$

$$\mathbf{J}^2|ljK\rangle = j(j+1)\hbar^2|ljK\rangle, \tag{3}$$

$$J_z|ljK\rangle = K\hbar|ljK\rangle, \tag{4}$$

and $j = l \pm \frac{1}{2}$. In the notation $|ljK\rangle$ we omitted the additional quantum numbers necessary to completely characterize the ket $|k\rangle$. Finally we denote by $\mathcal{R}_{lj}^{(k)}$ the radial part of the wave function of $|k\rangle$ coming from its component (l, j) (see next subsection for its explicit expression).

The corresponding DSD cross section takes the form of a sum of two coherent amplitudes [12,13]

$$\sigma^{(k)}(lj;LJ) = \frac{8\pi}{9}\frac{\mu}{\hbar^2}\left(\frac{k_\gamma}{k_n}\right)^3 \langle I_i K_i jK_f | I_f K_f\rangle^2 \times \left| T_d^{(k)}(lj;LJ) + T_s^{(k)}(lj;LJ)\right|^2, \tag{5}$$

where $T_d^{(k)}$ and $T_s^{(k)}$ denote the direct and semidirect amplitudes, respectively, μ is the reduced mass of the projectile-target system, and I_i is the angular momentum of the target with projection K_i on its intrinsic symmetry axis z. The direct contribution is given by

$$T_d^{(k)}(lj;LJ) = \bar{e}(-i)^{l+1} Z\left(LJlj;\tfrac{1}{2}1\right)\sqrt{S_{lj}^{(k)}}\left\langle \mathcal{R}_{lj}^{(k)}\middle| r\,|R_{LJ}\right\rangle, \tag{6}$$

where $\bar{e}$ is the effective charge ($\bar{e} = \mathrm{Ne}/A$ for proton and $\bar{e} = -\mathrm{Ze}/A$ for neutron), $S_{lj}^{(k)}$ is the spectroscopic factor, and $Z(LJlj;\frac{1}{2}1)$ is the Z coefficient [16]. As for the semidirect-capture amplitude, it is calculated as

$$T_s^{(k)}(lj;LJ) = \pm\frac{3}{2\langle r^2\rangle}\frac{N^2Z^2}{A^3}e\sum_{l'j'}\left[(-i)^{l'+1} Z\left(\mathrm{LJl'j'};\frac{1}{2}1\right)\right. \times \sqrt{S_{l'j'}^{(k)}}\left\langle \mathcal{R}_{l'j'}^{(k)}\middle| h(r)|R_{LJ}\right\rangle \sum_\nu \langle 1,-\nu,J,\nu+K|j'K\rangle \left.\times \langle 1,-\nu,J,\nu+K|jK\rangle \frac{|\langle\psi_{1\nu}|\rho'_\nu|\psi_{00}\rangle|^2}{E_n-(E_\nu+\epsilon_k)+i\frac{1}{2}\Gamma_\nu}\right], \tag{7}$$

where $\langle r^2\rangle$ is the mean square radius, $h(r)$ is the particle-vibration coupling function, ϵ_k is the single-particle energy of the considered bound state, E_ν and Γ_ν are the giant dipole resonance energy and width, and the index ν stands for the modes corresponding to major and minor axes. When $h(r)$ is a surface coupling function [12], the factor $3/\langle r^2\rangle$ must be omitted [17]. The transition matrix element between the dipole and ground states $\langle\psi_{1\nu}|\rho'_\nu|\psi_{00}\rangle$ can be related to a photoabsorption cross section [12,13]. The GDR parameters are taken from experimental data, or they are calculated with a simple systematics [18] obtained from the experimental database.

Upon summing over all the bound states and their (l, j) components, we finally obtain the total DSD cross section

$$\sigma = \frac{8\pi}{9}\frac{\mu}{\hbar^2}\sum_{L,J}\sum_{k=1}^{N_{\mathrm{lev}}}\left[\left(\frac{k_\gamma}{k_n}\right)^3\sum_{i=1}^{N(k)}\langle I_i K_i jK_f|I_f K_f\rangle^2 \times \left|T_d^{(k)}\left(l_i^{(k)} j_i^{(k)};LJ\right) + T_s^{(k)}\left(l_i^{(k)} j_i^{(k)};LJ\right)\right|^2\right]. \tag{8}$$

In this expression the sum over i represents the $N(k)$ different components $(l_i^{(k)}, j_i^{(k)})$ of $|k\rangle$, and N_{lev} is the number of bound-state levels (taking into account the Kramers' degeneracy due to the time reversal symmetry in the considered even-even targets). From energy conservation we have the following relation between the neutron center-of-mass kinetic energy E_n, the neutron separation energy of the final nucleus $S_n^{(A+1)}$, the bound-state energy ϵ_k, and the energy of the emitted γ-ray $E_\gamma = \hbar c k_\gamma$

$$E_n = \frac{(\hbar k_n)^2}{2\mu} = \epsilon_k - \epsilon_{\mathrm{GS}} + E_\gamma - S_n^{(A+1)}, \tag{9}$$

where ϵ_{GS} is the energy of the lowest unoccupied single-particle state in the target nucleus. In the independent-particle approximation, the neutron separation energy of the final nucleus $S_n^{(A+1)}$ is simply the opposite of ϵ_{GS}, hence

$$E_\gamma = E_n - \epsilon_k, \tag{10}$$

that is

$$\frac{k_\gamma}{k_n} = \sqrt{\frac{E_n}{2\mu c^2}}\left(1 + \frac{|\epsilon_k|}{E_n}\right), \tag{11}$$

because $\epsilon_k < 0$ for bound states.

As we have seen the radial wave function of the scattering state is needed to calculate the amplitudes in Eqs. (6) and (7). Here it is calculated with the global optical potential of Koning and Delaroche [19].

The semidirect capture cross section strongly depends on the particle-vibration coupling function $h(r)$ in Eq. (7). Boisson and Jang [12] adopted $h(r)$ in the form $V_1 df(r)/dr$, where $f(r)$ is the Woods-Saxon form and V_1 is the coupling strength that is often approximated by the depth of isospin term in the optical potential. In Ref. [12], $V_1 = 170$ MeV was employed, and this value is very close to the global optical potential of Koning and Delaroche [19], which is 168 MeV. Kitazawa *et al.* [13] adopted a different form, namely

$V_1 rf(r)$ with $V_1 = 110$ MeV. In contrast with these real form factors, Potokar [20] proposed a complex function of the form $V_1 rf(r) - 4iW_1 ardf(r)/dr$ and found, by analyzing the ^{208}Pb(n,γ) reaction, $V_1 = 75$ and $W_1 = 140$ MeV. Because this complex function is supported by the work of Likar and Vidmar [7], we employ it here with the same parameters V_1 and W_1 for all the considered nuclei, namely ^{208}Pb, ^{122,132}Sn, and ^{238}U.

B. Radial wave-function and spectroscopic factors within the Hartree-Fock-BCS approach

We consider here two different parametrizations with the traditionally corresponding pairing interactions. On the one hand, with the SLy4 parametrization [21] of the Skyrme interaction, adjusted to nuclear masses, charge radii, and some properties of nuclear matter, we use the density-dependent delta interaction (DDDI) of Duguet, Bonche, and Heenen [22] as a pairing interaction, successful in reproducing rotational bands in rare earths and actinide nuclei. On the other hand, the seniority force (constant matrix elements between paired of time reversed states) is chosen as a pairing interaction while using the Skyrme SIII [23] parametrization in the mean-field channel. The strengths of the seniority force for neutrons and protons retained here are the same as those used in the fission studies of Ref. [24] in the actinide region and Ref. [25] in the $A = 70$ mass region.

Within the Hartree-Fock-BCS approach, the ground state $|\Psi\rangle$ of an even-even nucleus takes the form

$$|\Psi\rangle = \prod_{k>0}\left(u_k + v_k a_k^\dagger a_{\bar{k}}^\dagger\right)|0\rangle, \tag{12}$$

where $|\bar{k}\rangle$ is the time-reversed conjugate of $|k\rangle$ and $a_k^\dagger$ is the single-particle state creation operator. The BCS variational parameters u_k and v_k are related through $u_k^2 + v_k^2 = 1$, v_k^2 representing the occupation probability of $|k\rangle$, and this relation ensures that $|\Psi\rangle$ is normalized to unity. The single-particle wave function $\phi_k(\mathbf{r},\sigma,\tau)$ associated with $|k\rangle$, where σ and τ denote to spin and isospin degrees of freedom, respectively, is solution to the Skyrme-Hartree-Fock equation [26,27]

$$\left[-\nabla\cdot\frac{\hbar^2}{2m_\tau^*(\mathbf{r})}\nabla + U_\tau(\mathbf{r}) - i\mathbf{W}_\tau(\mathbf{r})\cdot(\nabla\times\sigma)\right]\phi_k(\mathbf{r},\sigma,\tau) = \epsilon_k\phi_k(\mathbf{r},\sigma,\tau), \tag{13}$$

where $m_\tau^*(\mathbf{r})$ is the nucleon effective mass, $U_\tau(\mathbf{r})$ is the central potential, and $\mathbf{W}_\tau(\mathrm{r})$ is the spin-orbit coupling potential. These three quantities depend on all single-particle wave functions, which makes this approach self-consistent. Once the single-particle eigenvalues of Eq. (13) are calculated, they are used to solve the BCS gap equation from which the occupation factors v_k are determined, and the Hartree-Fock Hamiltonian (through the three above quantities) is reconstructed and diagonalized again. This procedure is repeated until the single-particle wave functions ϕ_k converge.

In practice, owing to the axial symmetry assumed here, Eq. (13) is solved by diagonalization of the Skyrme-Hartree-Fock Hamiltonian in the cylindrical harmonic-oscillator basis $\{|n_z n_\perp \Lambda\rangle\Sigma\}$ with the notation of Ref. [27]

$$|k\rangle = \sum_{n_z\geqslant 0}\sum_{n_\perp\geqslant 0}\sum_{\Sigma=\pm 1/2} c^{(k)}_{n_z n_\perp \Lambda_k \Sigma}|n_z n_\perp \Lambda_k \Sigma\rangle. \tag{14}$$

This infinite basis is truncated by using the prescription of Ref. [28] in which all the basis states $|n_z n_\perp \Lambda\Sigma\rangle$ that satisfy the following condition are retained

$$\hbar\omega_\perp(n_\perp + 1) + \hbar\omega_z\left(n_z + \tfrac{1}{2}\right) \leqslant \hbar\omega_0(N_0 + 2), \tag{15}$$

with $\omega_0^3 = \omega_z\omega_\perp^2$. The basis, including the truncation condition, has therefore three parameters ω_z, $\omega_\perp$, and N_0. Introducing the deformation parameter q and the oscillator parameter b defined by

$$q = \frac{\omega_\perp}{\omega_z} \tag{16}$$

and

$$b = \sqrt{\frac{m\omega}{\hbar}}, \tag{17}$$

where m denotes the neutron and proton masses (assumed to be equal), we can rewrite Eq. (15) with only two parameters

$$q^{\frac{1}{2}}(n_\perp + 1) + q^{-\frac{2}{3}}\left(n_z + \tfrac{1}{2}\right) \leqslant N_0 + 2. \tag{18}$$

Given the variational character of the Hartree-Fock approximation, the best ground state $|\Psi\rangle$ of Eq. (12) corresponds to the set of single-particle state solutions of Eq. (13) that leads to the lowest value of the expectation value of the Skyrme-Hartree-Fock many-body Hamiltonian H. Consequently, for a given number of major shells N_0 (i.e., a given basis size), we have to optimize the basis parameters q and b so as to minimize the energy $\langle\Psi|H|\Psi\rangle$.

Then the cylindrical basis $\{|n_z n_\perp \Lambda\Sigma\rangle\}$ is expanded in the spherical harmonic-oscillator basis $\{|nljK\rangle\}$ with usual notation (n representing the number of nodes excluding the origin and infinity), which yields

$$|k\rangle = \sum_{n\geqslant 0}\sum_{l,j} s^{(k)}_{nlj}|nljK\rangle \tag{19}$$

with

$$s^{(k)}_{nlj} = \sum_{n_z,n_\perp,\Sigma} c^{(k)}_{n_z n_\perp \Lambda_k \Sigma}\langle nljK|n_z n_\perp \Lambda_k \Sigma\rangle, \tag{20}$$

where $\Lambda_k = K - \Sigma$. The overlaps $\langle nljK|n_z n_\perp \Lambda_k \Sigma\rangle$ are explicitly given in the Appendix. We can therefore express the coefficients $C^{(k)}_{lj}$ in Eq. (1) as

$$\left|C^{(k)}_{lj}\right|^2 = \sum_{n\geqslant 0}\left|s^{(k)}_{nlj}\right|^2. \tag{21}$$

Finally, if we call $R_{nl}(r)$ the radial part of the spherical harmonic-oscillator wave function (normalized to unity), then we can define the radial part $\mathcal{R}^{(k)}_{lj}$ of the (l,j) component of the wave function ϕ_k by

$$\mathcal{R}^{(k)}_{lj}(r) = \sum_{n\geqslant 0} s^{(k)}_{nlj} R_{nl}(r). \tag{22}$$

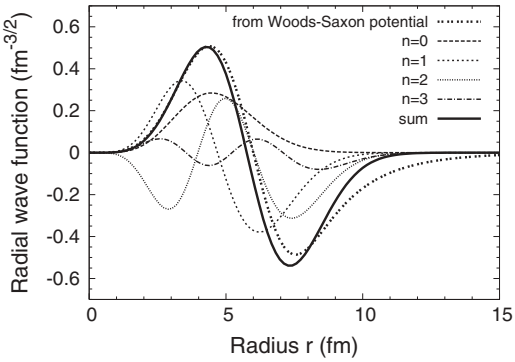

FIG. 1. Radial wave-function of the $g_{9/2}$ state in ^{208}Pb. The thin curves are the decomposition in the spherical harmonic-oscillator basis, and the thick solid curve is the sum of each component from the Skyrme-Hartree-Fock-BCS calculation. The thick-dotted curve corresponds to the radial wave function obtained with the Woods-Saxon potential.

We use a definition of the spectroscopic factor $S_{lj}^{(k)}$ that incorporates the expansion coefficients $C_{lj}^{(k)}$ to be consistent with Refs. [14,29]. We generalize the definition adopted by Vergnes and Sheline [29] by including pairing correlations as in Refs. [9,10] and write $S_{ij}^{(k)}$ for a capture reaction on an even-even target as

$$S_{lj}^{(k)} = \frac{2u_k^2}{2j+1}\left|C_{lj}^{(k)}\right|^2. \tag{23}$$

Before closing this section, we illustrate in Fig. 1 the expansion of the radial wave-function of the $g_{9/2}$ neutron state of ^{208}Pb with the SIII interaction.

This single-particle state has four major contributions from $n = 0$ to $n = 3$. These results are compared in Fig. 1 with those obtained by solving the Schrödinger equation for the Woods-Saxon potential, which is often used for the DSD capture calculations. As can be seen the HFBCS and Woods-Saxon radial wave functions are in very close agreement for a radius r up to about 8 fm, but beyond this range the HFBCS wave function vanishes much faster. This is a due to the choice of a harmonic-oscillator basis for the diagonalization of the Hartree-Fock Hamiltonian, giving a Gaussian-times-polynomial asymptotic behavior, whereas the expected behavior is exponential as exhibited by the Woods-Saxon solution. As a single-particle state becomes less and less bound, the difference between the true and the HFBCS asymptotic behaviors increases. It is likely that the radial integrals contributing to the direct and semidirect amplitudes involve a cancellation between internal and external capture. However, it is not clear whether improving the tails of the single-particle wave functions would significantly affect the results, given that we sum over all the bound states. A possible way of improving this asymptotic behavior would be to use the transformed harmonic-oscillator basis proposed by Stoitsov *et al*. [30].

III. RESULTS AND DISCUSSION

A. Bound-state properties

To avoid any confusion in the definition of the spectroscopic factor, we compare the calculated occupation probabilities v_k^2 for various bound states with the values extracted from experimental data for five even isotopes of tin from ^{116}Sn to ^{124}Sn. These nuclei being found spherical, there is no ambiguity in the assignment of the quantum numbers l and j to the single-particle states $|k\rangle$. The results obtained with the SLy4 Skyrme interaction and the DDDI pairing interaction are shown in Table I, and those obtained with the SIII parametrization and the seniority pairing force in Table II.

The overall agreement is fair within the HFBCS model using the SLy4 interaction in the mean-field channel and the DDDI interaction in the pairing channel, noted HF(SLy4)+BCS(DDDI), even very good for the $g_{7/2}$ level, and the HF(SIII)+BCS(G) results, obtained using the SIII interaction in the mean-field channel and the seniority force in the pairing channel, are in very good agreement with the experimental values for the five isotopes, especially for the ^{122,124}Sn nuclei. A more detailed comparison reveals a general trend that can be connected with the pairing strength. Indeed, let us assume that v_k^2 decreases as the state $|k\rangle$ gets less and less bound at a rate varying in the opposite way of the pairing strength. For the sake of argument we approximate v_k^2 by a Fermi function

$$v_k^2(\epsilon) \approx \left[1 + \exp\left(\frac{\epsilon - \epsilon_F}{\delta}\right)\right]^{-1}, \tag{24}$$

where the diffuseness δ is an increasing function of the pairing strength and ϵ_F denotes the energy of the Fermi level (last occupied level in a pure Hartree-Fock picture). From Table I the occupation probability of the states below the Fermi level

TABLE I. Occupation probabilities of five neutron single-particle levels in the $N = 50 - 82$ shell for even Sn isotopes within the HF(SLy4)+BCS(DDDI) approach. Experimental data are taken from Ref. [10].

Level	^{116}Sn		^{118}Sn		^{120}Sn		^{122}Sn		^{124}Sn	
	Th.	Exp.	Th.	Exp.	Th.	Exp.	Th.	Exp.	Th.	Exp.
$h_{11/2}$	0.12	0.27	0.15	0.33	0.21	0.35	0.35	0.47	0.45	0.55
$d_{3/2}$	0.36	0.25	0.50	0.33	0.66	0.55	0.74	0.59	0.83	0.68
$s_{1/2}$	0.60	0.42	0.74	0.50	0.84	0.61	0.85	0.69	0.90	0.74
$g_{7/2}$	0.79	0.78	0.87	0.86	0.92	0.89	0.92	0.92	0.95	0.95
$d_{5/2}$	0.94	0.79	0.96	0.80	0.97	0.87	0.96	0.86	0.97	0.93

TABLE II. Same as Table I within the HF(SIII)+BCS(G) model.

Level	^{116}Sn		^{118}Sn		^{120}Sn		^{122}Sn		^{124}Sn	
	Th.	Exp.	Th.	Exp.	Th.	Exp.	Th.	Exp.	Th.	Exp.
$h_{11/2}$	0.16	0.27	0.24	0.33	0.33	0.35	0.44	0.47	0.54	0.55
$d_{3/2}$	0.23	0.25	0.33	0.33	0.44	0.55	0.54	0.59	0.65	0.68
$s_{1/2}$	0.35	0.42	0.46	0.50	0.56	0.61	0.64	0.69	0.72	0.74
$g_{7/2}$	0.90	0.78	0.93	0.86	0.95	0.89	0.96	0.92	0.97	0.95
$d_{5/2}$	0.90	0.79	0.93	0.80	0.94	0.87	0.96	0.86	0.97	0.93

tends to be overestimated whereas the opposite is true for the levels above ϵ_F. Consequently, leaning on Eq. (24), we deduce that the strength of the pairing interaction DDDI retained here is too low to account for the observed diffuseness. Even though an adjustment of the pairing strength for each nucleus would improve the agreement for the occupation probabilities, we prefer to adopt here a more predictive approach by keeping the same pairing strength for all the considered nuclei, namely the one proposed by Duguet, Bonche, and Heenen [22].

Another bound-state property important in the DSD cross section is the single-particle energy. Some data are available only for two of the five nuclei considered, namely the doubly magic nuclei ^{208}Pb [31] and ^{132}Sn [32]. For the latter we actually consider the low-lying states of ^{133}Sn as single-neutron states of ^{132}Sn, which amounts to the independent-particle approximation (residual interaction neglected). In particular, according to the previously invoked approximation, we assume that $\epsilon_{f_{7/2}} = -S_n(^{133}\text{Sn}) = -2.42$ MeV. Figures 2 and 3 show calculated and experimental neutron single-particle energies for ^{208}Pb and ^{132}Sn, respectively.

We recall that the pairing correlations are vanishing for these magic nuclei, at least in the BCS approach, so the two HFBCS models differ here only by the Skyrme interaction used. Moreover, to make a quantitative comparison of the calculated and experimental single-particle level schemes we should include effects of coupling to more complicated configurations (especially particle-vibration coupling [33]), which is beyond the scope of the present work. However, we can note that, apart from a couple inversions, the calculated ordering is correct with both Skyrme interactions. More precisely, in the ^{208}Pb case, the only inversion with the SLy4 interaction occurs for the $g_{7/2}$ and $s_{1/2}$ levels, whereas two inversions occur with the SIII interaction ($f_{5/2} - p_{3/2}$ and $s_{1/2} - g_{7/2}$). The relevant bound states for the ^{208}Pb(n,γ) reaction cross section are those above the $p_{1/2}$ level (particle states) that have a negative energy. Therefore the cross section is calculated with only four levels for both interactions ($g_{9/2}, i_{11/2}, j_{15/2}$ and $d_{5/2}$), as compared to seven contributing experimental bound states. This may lead to an underestimate of the DSD capture cross section depending on the degree of compensation owing to the under-bound character of the above four single-particle levels. As for ^{132}Sn, the first unoccupied level is well reproduced, but the three next ones are calculated to be unbound (between 0 and 1 MeV) in contrast to experiment.

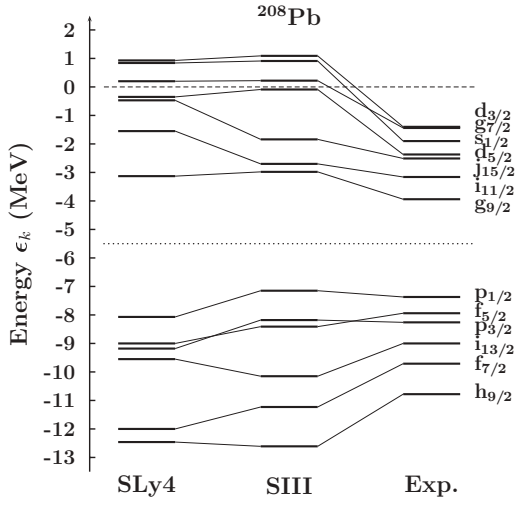

FIG. 2. Neutron single-particle level scheme in ^{208}Pb. The dotted line separates the hole states (below) from the particle states (above).

B. Capture cross section for spherical targets

First we perform the DSD model calculation with HFBCS bound states for the spherical, doubly magic target nucleus ^{208}Pb. Because of the vanishing pairing correlations (at least in the BCS approach), the only bound states accessible to the incident neutron are those lying above the Fermi level, for which the u_k^2 factor is maximum with $u_k^2 = 1$. The same treatment was also made by Longo and Saporetti [17]. The GDR parameters $E_0 = 13.6$ MeV, $\Gamma_0 = 3.78$ MeV, and $\sigma_0 = 541$ mb are taken from Ref. [12].

In Fig. 4 we have represented the direct (dashed line, $\sigma \propto \sum |T_d|^2$) and semidirect (dotted line, $\sigma \propto \sum |T_s|^2$) contributions obtained with the SLy4 bound states, together with the total capture cross section (solid line, $\sigma \propto \sum |T_d + T_s|^2$).

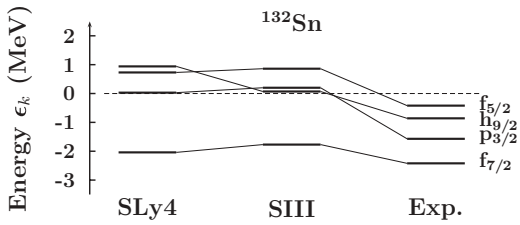

FIG. 3. Same as Fig. 2 for ^{132}Sn (states above the Fermi level only).

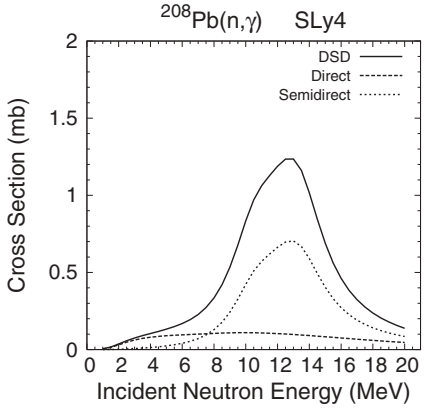

FIG. 4. Direct-semidirect neutron capture cross section for ^{208}Pb with the Potokar particle-vibration coupling function and the HF(SLy4)+BCS(DDDI) bound states. The direct and semidirect components are displayed as dashed and dotted lines, respectively.

Whereas the direct component is rather small but fairly constant over the considered energy range (1 to 20 MeV), the semidirect one is peaked around $E_\nu + \epsilon_k$. Moreover, as already noticed by Boisson and Jang [12], the interference term between the direct and the semidirect amplitudes is rather large. This conclusion does not depend on the nuclear structure model implemented to calculate the bound states.

The comparison of the DSD cross section calculated using SLy4 (solid line) and SIII (dashed line) bound states with the experimental data is shown in Fig. 5.

The calculated cross section has a shape consistent with the experimental data [34–36], but the absolute cross section is slightly lower. A better reproduction of the data might be obtained with an appropriate adjustment of the V_1 and W_1 parameters of the Potokar particle-vibration coupling function. Two other causes to the underestimate of the cross section are the underbound character of the calculated bound states and correlatively the missing experimental bound states calculated to be quasi bound. If we correct the calculations by including the latter states and shifting all the considered single-particle states so as to reproduce the experimental $g_{9/2}$ binding energy, we obtain the solid and dashed lines of Fig. 6, corresponding

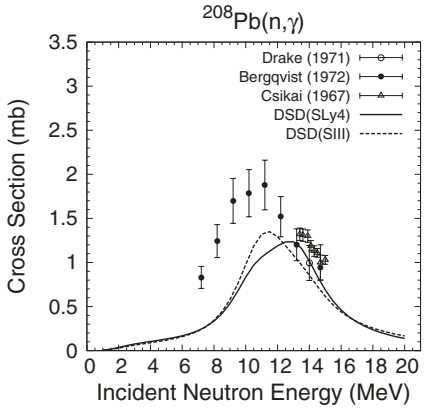

FIG. 5. Direct-semidirect neutron capture cross section for ^{208}Pb with bound states calculated within two different HFBCS models.

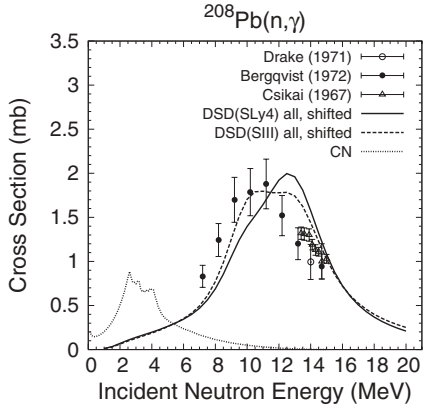

FIG. 6. Neutron capture cross section for ^{208}Pb. The DSD cross section is calculated with SLy4 (solid line) and SIII (dashed line) bound states. All the experimental bound states above the Fermi level are included and they are shifted so that the calculated $g_{9/2}$ energy equals the experimental one. The compound nucleus cross section is indicated by the dotted line.

to the SLy4 and SIII results, respectively. The agreement with the data becomes very good over the energy range spanned by the data, with a slight underestimate below 10 MeV. It is interesting to compare with Hauser-Feshbach-Moldauer calculations (dotted line in Fig. 6) for which the model parameters used are the optical potential of Koning and Delaroche [19] together with the level density parameters of Kawano, Chiba, and Koura [37]. The compound-nucleus (CN) reaction mechanism dominates up to 5 MeV only, beyond which the DSD mechanism takes over. The total cross section being the sum of the CN and DSD contributions, we deduce that the calculated total capture cross section below 10 MeV is in excellent agreement with measurements.

We have also performed capture cross section calculations for two tin isotopes, ^{122}Sn and ^{132}Sn (see Fig. 7).

The latter is of particular importance in the r process of nucleosynthesis. Similar to the ^{208}Pb case in Fig. 6, ^{132}Sn has a very small compound radiative-capture cross section due to the doubly magic nature, and reaction rates for the ^{132}Sn(n, γ) and ^{133}Sn(γ, n) reactions become comparable in the r process. As a result, relatively large amount of ^{132}Sn accumulates before it β decays to ^{132}Sb.

Given the doubly magic character of ^{132}Sn, the pairing correlations are vanishing for this nucleus, at least in the BCS approach, in contrast with ^{122}Sn for which we find a significant depopulation of hole states due to pairing correlations. In the case of ^{122}Sn neutrons can thus be captured by particle states (above the Fermi level) as well as hole states (below the Fermi level). The compound-nucleus cross sections are calculated with the Hauser-Feshbach-Moldauer theory. Because the average radiative width Γ_γ for these isotopes are not reported, we estimated the Γ_γ values in a simple way. The Γ_γ values for ^{119}Sn and ^{120}Sn are 0.1 and 0.036 eV, respectively [38]. Because it is empirically known that Γ_γ has a weak mass-number dependence, we estimated $\Gamma_\gamma = 0.08$ eV for ^{120}Sn, which roughly reproduces the experimental capture cross sections in the upper panel of Fig. 7, although they are scattered. The Γ_γ value of 0.1 eV was estimated for ^{132}Sn from

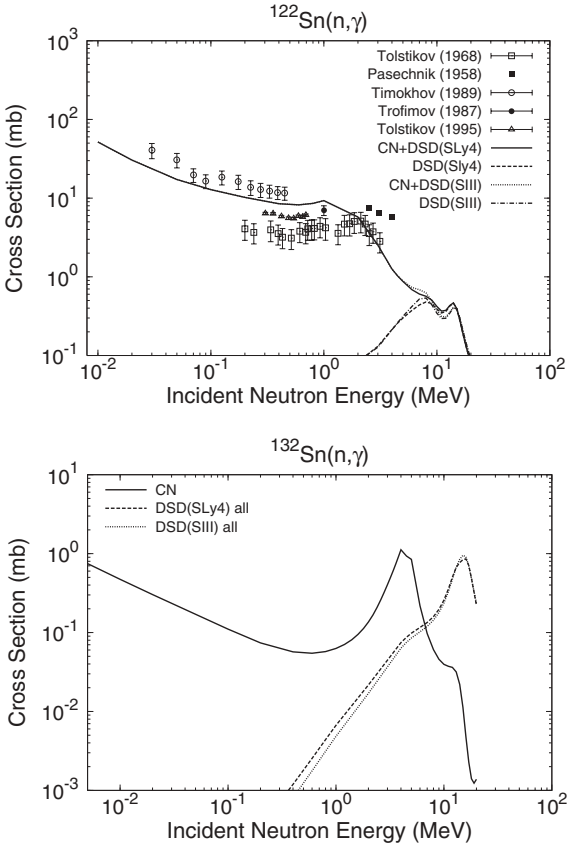

FIG. 7. Same as Fig. 5 for two tin isotopes: ^{122}Sn (upper panel) and doubly magic ^{132}Sn (lower panel). The curves labeled "all" correspond to calculations that include all the calculated single-particle states experimentally bound (determined in the Koopmans' approximation from ^{133}Sn experimental low-lying states).

a systematic study of the Γ_γ values, which gives the compound capture cross section shown by the solid curve in the lower panel of Fig. 7. Note that the calculated compound capture cross sections on ^{132}Sn are very small, and the calculation may have large uncertainties.

In the upper panel we have represented the DSD cross sections with SLy4 and SIII as dashed and dash-dotted lines, respectively, and the corresponding CN+DSD cross sections as solid and dotted lines, respectively, for ^{122}Sn. The DSD contribution to this cross section below 10 MeV is small, and the experimental data [39–43] below 4 MeV are purely reproduced by the compound reaction mechanism. Above 10 MeV the DSD mechanism becomes dominant. It is interesting to note that both Skyrme interactions give very similar DSD results for this isotope.

In the lower panel of Fig. 7 we have plotted the calculated CN capture cross section (solid line) as well as the DSD cross sections obtained with SLy4 (dashed line) and SIII (dotted line) single-particles for the ^{132}Sn target. All levels experimentally bound have been included with their unshifted energies (i.e., the four levels represented in Fig. 3 for SLy4 and SIII). The large peak near $E_n = 4$ MeV is because the neutron inelastic channels are closed below 4 MeV. The DSD cross sections become almost in the same magnitude in the MeV incident energy region, and it may change the Maxwellian averaged cross section (MACS) when the temperature of the r process is very high. As mentioned, the compound capture cross section on ^{132}Sn is sensitive to the reaction model parameters used. In the case we predict the CN cross section lower, the DSD contribution to the MACS will be more important.

C. Capture cross section for the deformed target ^{238}U

The Skyrme-HFBCS approach was applied to actinides to investigate fission properties from the potential-energy surface (see, e.g., Ref. [44]). Here we adopt the same model for ^{238}U to determine the single-particle states and their occupation probabilities. Because ^{238}U is a strongly deformed nucleus, coupled-channels calculations for the scattering states are expected to be more appropriate. However, we make the approximation of a spherical optical model and use the Koning-Delaroche potential [19] to generate the scattering waves. The GDR parameters are taken from Caldwell *et al.* [45] and the coupling strength was the same as the ^{208}Pb calculation, namely $V_1 = 75$ and $W_1 = 140$ MeV.

Figure 8 shows a comparison of the calculated DSD cross section obtained using SLy4 (solid line) and SIII (dashed line) deformed bound states with the experimental data [15,35].

The use of SLy4 bound states gives a slightly better agreement with measurements. In their calculations McDaniels *et al.* [15] adopted similar particle-vibration coupling parameters but obtained systematically lower results, for example 0.7 mb at 12 MeV, which is 40 to 50% lower than in our calculations. They attributed this underestimate to the direct part of the cross section. The direct cross section of Boisson and Jang [12] is 0.46 mb at 14 MeV, and our value is 1.06 mb with SLy4 and 1.39 mb with SIII. McDaniels *et al.* [15] reported that their value was similar to that of Boisson and Jang [12], and they noted that this lower cross section was due to their spherical approximation for the bound states. However our calculations (dotted and dash-dotted lines in Fig. 8) indicate that the effect of the target deformation is rather small. This can be explained by the fact that the sets of bound states in the spherical and deformed HFBCS solutions that contribute to the direct and semidirect amplitudes do not differ significantly in proportion

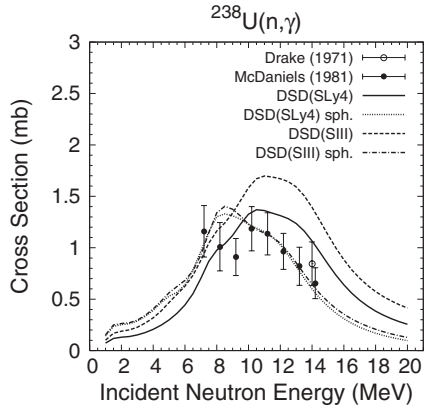

FIG. 8. Same as Fig. 5 for the deformed target ^{238}U with unshifted single-particle energies.

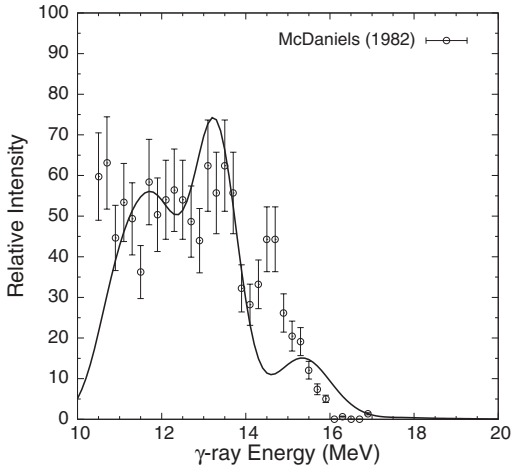

FIG. 9. Comparison of experimental and calculated (solid line) γ-ray spectra at the neutron incident energy of 10.7 MeV for ^{238}U. The theoretical spectrum is Gaussian-broadened with 500 keV width.

to the number of contributing bound states. The differences lie essentially in the nuclear single-particle level densities. Therefore it seems to us that the better agreement of our DSD cross section obtained using spherical bound states (dotted and dash-dotted lines in Fig. 8 for SLy4 and SIII, respectively) with experimental data from 10 to 14 MeV, regardless of the Skyrme interaction used, is fortuitous. It is worth adding that the rescaling of single-particle energies in the deformed case as done in the previous subsection for ^{208}Pb would have virtually no effect for ^{238}U given the high level density.

In Fig. 9 we compare our calculated γ-ray spectrum with the experimental data [15] at $E_n = 10.7$ MeV. Because experimental response function is not available, we broadened the calculated γ-ray spectrum using Gaussian with 500 keV half-width, and the calculated curve was renormalized arbitrarily to the experimental data. Our calculation reproduces the gross structure of the experimental data, except for a peak location. The peak near 15 MeV in the calculation is from γ rays to the single-particle levels near the Fermi energy and probably corresponds to the 14.5 MeV peak in the experimental data. The energy difference between the experimental data and calculation is due to uncertainty in the calculated single-particle energies, which are sensitive to the effective two-body interaction used.

Before concluding we would like to add that the extension to odd targets could be done in the following approximate way. First the target angular momentum I_i can be accounted for by summing over all contributions obtained by considering the initial single neutron as a spectator and applying the same expression of $\sigma^{(k)}(lj;LJ)$ as for an even target, namely Eq. (5). Then we have to multiply the resulting cross section by the usual spin statistical factor $(2j+1)/[2(2I_i+1)]$ and sum over the single-particle states k and (L, J). In this case the spectroscopic factor takes the form

$$S_{lj}^{(k)} = 2v_k^2\left(C_{lj}^{(k)}\right)^2. \tag{25}$$

IV. CONCLUSION

We proposed a new technique to calculate the DSD nucleon capture cross sections. The single-particle bound states and their occupation probabilities are determined within the HFBCS model, whereas the incident wave function is calculated in the optical model. The transition amplitudes are calculated for each single-particle state using the theory of Boisson and Jang [12], which is an extension of the DSD theory for deformed nuclei. The procedure adopted in this study does not require experimental spectroscopic factors, which are often inaccessible for nuclei of astrophysical interest. The calculated occupation probabilities for even tin isotopes from ^{116}Sn to ^{124}Sn prove to be in fairly good agreement with experimental data. The calculated neutron capture cross sections for ^{208}Pb and ^{238}U reproduce very well the experimental data available when the Potokar's complex form factor for the vibration-particle coupling was used. The coupling strengths, V_1 and W_1, are the only adjustable parameters in our method. However, a common set of V_1 and W_1 give a good fit to ^{208}Pb and ^{238}U cross sections simultaneously. The method was also applied to calculate neutron capture cross sections on ^{122}Sn and ^{132}Sn, which are important for the r process. For the ^{122}Sn case, the compound reaction is still dominant at the few MeV neutron incident energies. However, it is found that the DSD process becomes of the same magnitude for ^{132}Sn.

Because the incident wave function is calculated in a spherical potential, a natural extension of this study would be to perform calculations in the coupled-channel approach for both continuum and bound states, analogous to calculations for stripping reactions using the coupled-channel Born approximation (see, e.g., Refs. [46–48]).

ACKNOWLEDGMENTS

One of us (T. W.) acknowledges the Theoretical Division at LANL for the excellent working conditions extending to him during his visit. This work has been carried out under the auspices of the National Nuclear Security Administration of the U.S. Department of Energy at Los Alamos National Laboratory under contract no. DE-AC52-06NA25396.

APPENDIX

The notations in use here for the cylindrical harmonic-oscillator basis states $|n_z n_\perp \Lambda\Sigma\rangle$ and the spherical harmonic-oscillator basis states $|nlj\Omega\rangle$ are those introduced in Sec. II.

A. Transformation from cylindrical to spherical harmonic-oscillator basis without spin

To expand the cylindrical state $|n_z n_\perp \Lambda\rangle$ on the basis formed by the spherical states $|nl\Lambda\rangle$, we proceed in two steps. First we expand the one-dimensional harmonic-oscillator state $|n_z\rangle$ associated with the frequency ω_z on the same states associated with the frequency $\omega_\perp$. Then we can easily expand $|n_z n_\perp \Lambda\rangle$ on the spherical basis states $|nl\Lambda\rangle$ because they all correspond to the same oscillator frequency $\omega_\perp$.

1. Relation between one-dimensional harmonic-oscillator states of different frequencies

The expansion of the one-dimensional harmonic oscillator basis states $|n_z(\omega_z)\rangle$ associated with the frequency ω_z on the same basis associated with the frequency ω_z' has been shown by Talman [49] to take the following form :

$$|n_z(\omega_z)\rangle = \sum_{\substack{n_z' \geqslant 0 \\ n_z - n_z' \text{even}}} A_{n_z n_z'}(q) |n_z'(\omega_z')\rangle \tag{A1}$$

with the overlap function:

$$A_{nn'}(q) = \sqrt{2^{n-n'} n! n'!} \left(\frac{q-1}{q+1}\right)^{\frac{n'-n}{2}} \left(\frac{2\sqrt{q}}{q+1}\right)^{n+\frac{1}{2}} \times \sum_{\nu=0}^{\left[\frac{n}{2}\right]} \frac{(-1)^\nu}{\nu! \left(\nu + \frac{n'-n}{2}\right)! (n-2\nu)!} \left(\frac{q-1}{4\sqrt{q}}\right)^{2\nu}, \tag{A2}$$

where $[x]$ denotes the integer part of x and $q = \omega_z'/\omega_z$. In practice, one truncates the infinite sum in Eq. (A1) when the square of the norm of $|n_z(\omega_z\rangle$

$$\langle n_z(\omega_z)|n_z(\omega_z)\rangle = \sum_{\substack{n_z' \geqslant 0 \\ n_z - n_z' \text{even}}} \left|A_{n_z n_z'}(q)\right|^2 \tag{A3}$$

is as close to 1 as desired.

2. Relation between cylindrical and spherical states with the same frequency

If the oscillator frequencies in the z direction ω_z and in the plane perpendicular to the z-axis $\omega_\perp$ are equal, it becomes easy to expand $|n_z(\omega_z) n_\perp(\omega_\perp)\Lambda\rangle$ on the basis states $|n(\omega_\perp) l \Lambda\rangle$ due to the spherical symmetry. According to Talman [49] we have

$$|n_z n_\perp \Lambda\rangle = \sum_{n,l} \delta_{n_z + n_\perp, 2n+l} B_{n_z, n_\perp, \Lambda; n, l} |n l \Lambda\rangle, \tag{A4}$$

where the overlap $B_{n_z n_\perp \Lambda, nl}$ has the following expression

$$B_{n_z, n_\perp, \Lambda; n, l} = (-1)^{\beta+n+\Lambda} 2^n \sqrt{\frac{\alpha!}{\beta!} \frac{n_z!}{2^{n_z}} \frac{(l-\Lambda)!}{(l+\Lambda)!} \frac{(2l+1)(n+l)!}{n!(2n+2l+1)!}} \sum_\lambda (-1)^\lambda \frac{[2(l-\lambda)]!(\lambda+n)!}{\lambda!(l-\lambda)![n_z - 2(\lambda+n-\beta)]!(\lambda+n-\beta)!} \tag{A5}$$

with the notations

$$\alpha = \frac{n_\perp + \Lambda}{2} \tag{A6}$$

$$\beta = \frac{n_\perp - \Lambda}{2}. \tag{A7}$$

It is important to note that the sum over λ in Eq. (A5) is finite because the factorials limit the range of possible values of λ. However the sums over n and l in Eq. (A4) run from 0 to ∞ and one has to truncate them. For the calculations of the present study, we have checked that the maximal values $n_{\max} = 10$ and $l_{\max} = 15$ are sufficient.

B. Orbital angular momentum and spin coupling

If we add the spin degree of freedom, the eigenstates of the spherical harmonic oscillator become:

$$|n l \Lambda \Sigma\rangle = |n l \Lambda\rangle \otimes |s \Sigma\rangle \tag{A8}$$

where $|s\Sigma\rangle$ is an eigenstate of the spin operators $\mathbf{S}^2$ with the eigenvalue $\frac{3}{4}\hbar^2$ and S_z with the eigenvalue $\Sigma\hbar$ ($\Sigma = \pm\frac{1}{2}$). The coupling of the two angular momenta $\mathbf{L}$ and $\mathbf{S}$ leads to the total angular momentum $\mathbf{J}$ and the coupled basis states $|nlj\Omega\rangle$ related to the uncoupled basis states $|nl\Lambda\Sigma\rangle$ through

$$|n l \Lambda \Sigma\rangle = \sum_j \left\langle l \Lambda \ \frac{1}{2} \Sigma \middle| \ j \Omega \right\rangle |n l j \Omega\rangle \tag{A9}$$

with $\Omega = \Lambda + \Sigma$. We therefore arrive at

$$\begin{aligned} &\langle n(\omega_\perp) l j \Omega | n_z(\omega_z) n_\perp(\omega_\perp) \Lambda \Sigma\rangle \\ &\quad = \delta_{n_z + n_\perp - 2n - l, \text{even}} A_{n_z 2n+l-n_\perp}(q) B_{2n+l-n_\perp, n_\perp, \Lambda; n, l} \\ &\qquad \times \left\langle l \Lambda \tfrac{1}{2} \Sigma \middle| \ j \Omega \right\rangle \end{aligned} \tag{A10}$$

with the deformation parameter $q = \omega_\perp/\omega_z$.

[1] R. L. Macklin and J. H. Gibbons, Rev. Mod. Phys. **37**, 166 (1965).
[2] R. Rauscher, F.-K. Thielemann, and K.-L. Kratz, Nucl. Phys. **A621**, 331c (1997).
[3] R. Rauscher and F.-K. Thielemann, At. Data Nucl. Data Tables **75**, 1 (2000).
[4] G. E. Brown, Nucl. Phys. **57**, 339 (1964).
[5] C. F. Clement, A. M. Lane, and J. R. Rook, Nucl. Phys. **66**, 273 (1965).
[6] W. E. Parker, M. B. Chadwick, F. S. Dietrich, J. E. Kammeraad, S. J. Luke, K. E. Sale, R. M. Chasteler, M. A. Godwin, L. H. Kramer, G. J. Schmid, H. R. Weller, and A. K. Kerman, Phys. Rev. C **52**, 252 (1995).
[7] A. Likar and T. Vidmar, Nucl. Phys. **A591**, 458 (1995).

[8] S. Goriely, Phys. Lett. **B436**, 10 (1998).
[9] S. Yoshida, Phys. Rev. **15**, 2122 (1961).
[10] B. L. Cohen and R. E. Price, Phys. Rev. **121**, 1441 (1960).
[11] P. Möller, J. R. Nix, W. D. Myers, and W. J. Swiatecki, At. Data Nucl. Data Tables **59**, 185 (1995).
[12] J. P. Boisson and S. Jang, Nucl. Phys. **A189**, 334 (1972).
[13] H. Kitazawa, T. Hayase, and N. Yamamuro, Nucl. Phys. **A307**, 1 (1978).
[14] B. Pålsson, J. Krumlinde, I. Bergqvist, L. Nilsson, A. Lindholm, D. C. Santry, and E. D. Earle, Nucl. Phys. **A345**, 221 (1980).
[15] D. K. McDaniels, P. Varghese, D. M. Drake, E. Arthur, A. Lindholm, I. Bergqvist, and J. Krumlinde, Nucl. Phys. **A384**, 88 (1982).
[16] L. C. Biendenharn, J. M. Blatt, and M. E. Rose, Rev. Mod. Phys. **24**, 249 (1952); J. M. Blatt and L. C. Biedenharn, Rev. Mod. Phys. **24**, 258 (1952).
[17] G. Longo and F. Saporetti, Nucl. Phys. **A199**, 530 (1973).
[18] T. Belgya, O. Bersillon, R. Capote, T. Fukahori, G. Zhigang, S. Goriely, M. Herman, A. V. Ignatyuk, S. Kailas, A. Koning, P. Oblozinsky, V. Plujko, and P. Young, "Handbook for calculations of nuclear reaction data, RIPL-2," IAEA-TECDOC-1506 (IAEA, Vienna, 2006).
[19] A. Koning and J.-P. Delaroche, Nucl. Phys. **A713**, 231 (2003).
[20] M. Potokar, Phys. Lett. **B46**, 346 (1973).
[21] E. Chabanat, P. Bonche, P. Haensel, J. Meyer, and R. Schaeffer, Nucl. Phys. **A635**, 231 (1998).
[22] T. Duguet, P. Bonche, and P.-H. Heenen, Nucl. Phys. **A679**, 427 (2001).
[23] M. Beiner, H. Flocard, N. Van Giai, and P. Quentin, Nucl. Phys. **A238**, 29 (1975).
[24] L. Bonneau, P. Quentin, and D. Samsœn, Eur. Phys. J. A **21**, 391 (2004).
[25] L. Bonneau and P. Quentin, Phys. Rev. C **72**, 014311 (2005).
[26] D. Vautherin and D. M. Brink, Phys. Rev. C **5**, 626 (1972).
[27] D. Vautherin, Phys. Rev. C **7**, 296 (1973).
[28] H. Flocard, P. Quentin, A. Kerman, and D. Vautherin, Nucl. Phys. **A203**, 443 (1973).
[29] M. N. Vergnes and R. K. Sheline, Phys. Rev. **132**, 1736 (1963).
[30] M. V. Stoitsov, J. Dobaczewski, P. Ring, and S. Pittel, Phys. Rev. C **61**, 034311 (2000).
[31] C. H. Johnson, D. J. Horen, and C. Mahaux, Phys. Rev. C **36**, 2252 (1987).
[32] P. Hoff *et al.* and ISOLDE Collaboration, Phys. Rev. Lett. **77**, 1020 (1996).
[33] V. Bernard and N. Van Giai, Nucl. Phys. **A348**, 75 (1980).
[34] J. Csikai, G. Peto, M. Buczko, Z. Milligy, and N. Eissa, Nucl. Phys. **A95**, 229 (1967).
[35] D. Drake, I. Bergqvist, and D. K. McDaniels, Phys. Lett. **B36**, 557 (1971).
[36] I. Bergqvist, D. M. Drake, and D. K. McDaniels, Nucl. Phys. **A191**, 641 (1972).
[37] T. Kawano, S. Chiba, and H. Koura, J. Nucl. Sci. Technol. **43**, 1 (2006).
[38] S. F. Mughabghab, *Atlas of Neutron Resonances, Resonance Parameters and Thermal Cross Sections, Z=1–100* (Elsevier, Amsterdam, 2006).
[39] V. A. Tolstikov, V. P. Koroleva, V. E. Kolesov, A. G. Dovbenko, and Yu. N. Shubin, Atomnaya Energiya **24**, 576 (1968).
[40] M. V. Pasechnik, I. F. Barchuk, I. A. Totsky, V. I. Strizhak, A. M. Korolov, Yu. V. Hofman, G. N. Lovchikova, E. A. Koltynin, and G. B. Yankov, *Proceedings of the 2nd International Conference on the Peaceful Uses of Atomic Energy* (United Nations, Geneva, 1958), Vol. 15, p. 18.
[41] V. M. Timokhov, M. V. Bokhovko, A. G. Isakov, L. E. Kazakov, V. N. Kononov, G. N. Manturov, E. D. Poletaev, and V. G. Pronyaev, Obninsk Report FEI-1921 (1988); Yad. Fiz. **50**, 609 (1989)[Sov. J. Nucl. Phys. **50**, 375 (1989)].
[42] Yu. N. Trofimov, *Proc. 1st Int. Conf. on Neutron Physics*. (Kiev, 1987), Vol. 3, p. 331.
[43] V. A. Tolstikov, A. N. Davletshin, E. V. Teplov, and O. A. Tipunkov, Yad. Konst. **1992**, 41 (1992); **1994**, 46 (1994).
[44] L. Bonneau, Phys. Rev. C **74**, 014301 (2006).
[45] J. T. Caldwell, E. J. Dowdy, B. L. Berman, R. A. Alvarez, and P. Meyer, Phys. Rev. C **21**, 1215 (1980).
[46] N. Keeley, N. Alamanos, and V. Lapoux, Phys. Rev. C **69**, 064604 (2004).
[47] N. Austern, Y. Iseri, M. Kamimura, M. Kawai, G. Rawitscher, and M. Yahiro, Phys. Rep. **154**, 125 (1987).
[48] J. S. Al-Khalili and F. M. Nunes, J. Phys. G **29**, R89 (2003).
[49] J. D. Talman, Nucl. Phys. **A141**, 273 (1970).